

## Article

# Incorporation of Disposed Face Mask to Cement Mortar Material: An Insight into the Dynamic Mechanical Properties

Qiong Nie <sup>1,2</sup>, Bangbiao Wu <sup>3</sup>, Zheng Wang <sup>3,\*</sup>, Xiaoyan Dai <sup>1,2</sup> and Lingyun Chen <sup>1,2,4</sup>

<sup>1</sup> School of Building and Materials Engineering, Hubei University of Education, Wuhan 430205, China; qiongnie@hue.edu.cn (Q.N.); daixiaoyan@hue.edu.cn (X.D.); sukd2102619@segi4u.my (L.C.)

<sup>2</sup> Hubei BIM Intelligent Construction International Science and Technology Cooperation Base, Hubei University of Education, Wuhan 430205, China

<sup>3</sup> State Key Laboratory of Hydraulic Engineering Intelligent Construction and Operation, School of Civil Engineering, Tianjin University, Tianjin 300072, China; bbwu@tju.edu.cn

<sup>4</sup> Graduate School of Business, SEGi University, Petaling Jaya 47810, Selangor, Malaysia

\* Correspondence: wangz0699@tju.edu.cn

**Abstract:** Incorporating masks into building materials offers a potential solution to the environmental threat of disposable masks with promising material performance. However, research on their dynamic properties is lacking to further determine the application range of the new composite. This study addresses this gap by shredding face masks into strips and incorporating them into mortars at varying volume ratios. The integrity and compactness of the mortar was measured and characterized by P-wave velocity, while dynamic compression properties were explored using a split Hopkinson pressure bar (SHPB) system. Subsequently, sieve analysis was conducted on the fractured specimens. The results indicate that incorporating masks generally improves the mortar integrity and the fragmentation after impacting. The dynamic uniaxial compression strength (DUCS) decreased for all mixing designs compared to plain ones under a constant loading rate. Meanwhile, the dissipated energy density showed a similar trend to the P-wave velocity, exhibiting less pronounced enhancement at higher loading rates. According to the dynamic characteristics, a dynamic constitutive model based on the Lemaitre principle and Weibull distribution of damage is developed and validated. The test results are further understood through the perspective of the mechanism of mask inclusion.

**Keywords:** face mask; reinforced mortar; SHPB; dynamic uniaxial compressive strength; dissipated energy



**Citation:** Nie, Q.; Wu, B.; Wang, Z.; Dai, X.; Chen, L. Incorporation of Disposed Face Mask to Cement Mortar Material: An Insight into the Dynamic Mechanical Properties. *Buildings* **2024**, *14*, 1063. <https://doi.org/10.3390/buildings14041063>

Academic Editor: Elena Ferretti

Received: 6 March 2024

Revised: 3 April 2024

Accepted: 9 April 2024

Published: 11 April 2024



**Copyright:** © 2024 by the authors. Licensee MDPI, Basel, Switzerland. This article is an open access article distributed under the terms and conditions of the Creative Commons Attribution (CC BY) license (<https://creativecommons.org/licenses/by/4.0/>).

## 1. Introduction

The heightened awareness of protection has led to a significant increase in the use of personal protective equipment (PPE), consequently contributing to a surge in health-care solid waste production [1]. Disposable face masks, the most commonly used PPE, were estimated to be released into the environment at a staggering rate of 129 billion per month in 2020 [2,3]. Although mask mandates were lifted as COVID-19 transitioned to the epidemic phase, some people may choose to continue wearing masks for various reasons [4]. Comprising polypropylene fabrics (spun-bond polypropylene and melt-blown polypropylene) as their primary raw materials, these masks possess characteristics such as corrosion resistance and difficult degradation [5–7]. Moreover, they continuously release micro-plastics, nanoparticles and even heavy metals into the surrounding media during the use and disposal stages, exacerbating air and water pollution [8–10]. The disposal of this medical waste has attracted a great deal of attention. However, traditional methods like landfilling and incineration are unsuitable due to the potential risks of mask particles leaching into the environment and the release of toxic emissions. More efficient and greener waste disposal methods need to be developed urgently.

There have been a number of explorations into the proper treatment of mask waste. On the one hand, it is based on the structural properties of the mask material itself. As a polymer material, the disposal of masks through pyrolysis or chemical conversion is inherently feasible. For instance, the carbon source of the mask could be transformed into a dense hollow fiber porous structure through a one-step heat treatment following the sulfonation reaction [11]. The resulting product shows potential as an electrode material for high-performance supercapacitors. However, the implementation of these intricate techniques poses challenges due to strict environmental requirements and substantial upfront investments [12].

Another alternative is disposing masks by physical means. Incorporating fiber material for enhancement or other waste for disposal has been studied and applied extensively [13–16]. Polypropylene fiber is often selected due to its excellent corrosion resistance and tensile properties to obtain better concrete performance [17–19]. As a polypropylene product, disposable face masks share properties similar to those of fiber and plastic. Incorporating masks into cement-based building materials is thus explored, with a view to seal the masks without affecting the properties of the raw material. Saberian et al. [20] first incorporated a shredded face mask (SFM) with dimensions of 20 mm × 5 mm into a pavement's base/subbase material and conducted compaction tests and unconfined compression tests on the new mixture. The results demonstrated improvements in the dry density, uniaxial compressive strength, and resilient modulus. They later mixed the same SFM into concrete, observing similar enhancements in the compressive strength, tensile strength, and overall quality [7]. Idrees et al. [6] cut masks into squares with 1.5–2.0 mm side lengths, and found their inclusion enhanced the impermeability, corrosion resistance and compressive strength of the concrete, while slightly reducing the tensile strength. The incorporation of 1 cm square mask sheets was subsequently shown to increase tensile, compressive, and flexural strength while maintaining high quality and reducing slump [21]. However, when using larger mask pieces, the obtained conclusions changed. Paul et al. [22] found that incorporating mask strips with a median length of 42 mm and a 3 mm width reduced the concrete strength and workability. Maloba et al. [23] investigated the effect of different lengths (20–40 mm) and contents (1–5%) of mask strips on the properties of concrete. The results indicated a decrease in compressive strength with an increase in length and dosage content. Moreover, the potential for recycling masks in mortars was studied. Studies found that 2 cm<sup>2</sup> and 4 cm<sup>2</sup> mask fragments, as well as crushed face masks, could increase thermal resistance, the acoustic reflection coefficient and sorptivity while enhancing the compressive and flexural strength of the mortar [24,25].

The revealed properties of cement-based materials containing face masks showcase the feasibility of this disposal method at a certain content. However, previous studies predominantly concentrated on the workability and static mechanical properties of these materials. Few attempts have been made to investigate their dynamic performance. Civil engineering structures are subjected to transient loading, including impacts, explosions, earthquakes, etc. These scenarios imply that the dynamic compressive properties of the material are particularly crucial for safe design. Therefore, investigating the effect of mask doping on the dynamic compression characteristics of the material is another key task in assessing the feasibility of this disposal method.

In this study, shredded face masks (SFMs) of a relatively modest size (20 mm × 5 mm) were blended with sand, cement and other binding materials in varying volume percentages to produce mortar cylinder specimens [7,20,26]. P-wave velocity was measured to test the integrity of the mixtures. A dynamic uniaxial compression test was conducted using an SHPB system coupled with a momentum trap. Subsequently, sieve analysis was performed on the fractured specimens. The integrity, dynamic uniaxial compressive strength and dissipated energy density of mortar with different SFM inclusions were quantitatively analyzed. A constitutive model based on the Lemaitre principle and Weibull distribution was established and verified to describe the dynamic response of mortars. The objective of this work is to assess the feasibility of the mask disposal method from a dynamic perspective

and provide further insights into the application range of cement-based materials with mask inclusion.

## 2. Materials and Methods

### 2.1. Material Mixing and Specimen Preparation

The raw materials used to fabricate specimens are detailed in Table 1. Fly ash (main components:  $\text{Al}_2\text{O}_3$ –24.2%,  $\text{SiO}_2$ –45.1%,  $\text{CaO}$ –4.5%,  $\text{SO}_3$ –1.2%), mineral powder (main components:  $\text{SiO}_2$ –33%,  $\text{CaO}$ –39%,  $\text{Al}_2\text{O}_3$ –15%,  $\text{MgO}$ –10%,  $\text{SO}_3$ –2%) and silica fume were mixed to enhance the homogeneity and density [27,28]. To improve mortar integrity and workability, defoamer and water reducer were introduced [26]. The ordinary disposal surgical masks collected from a public source underwent meticulous disinfection measures, including alcohol spraying, exposure to sunlight for 3 h and heating to 70 °C for 1 h [29]. Subsequently, the metal strips and ear straps were manually removed. The layer component was then shredded into strips with a width of 5 mm and a length of 20 mm and incorporated into mixing with varying volume percentages of 0%, 0.1%, 0.2%, 0.3% and 0.5% (corresponding symbols FM0~FM5 in Table 1, respectively). It should be noted that this work is a basic exploration of the effect of masks on the dynamic properties of mortar materials. The size of the SFMs used in this study aligns with earlier research conducted by Kilmartin-Lynch et al. [7] and Saberian et al. [20]. In addition, with additional reference to the mass shares used by Ajam et al. [24], the SFM content was not designed in accordance with an arithmetic progression.

**Table 1.** Mortar mixing designs (unit: kg/m<sup>3</sup>).

Material	P.O 42.5 Cement	Standard Sand (ISO-6790)	Fly Ash	Silica Fume	Mineral Powder	Water	Water Reducing Agent	Defoamer	SFM
FM0									0
FM1									0.91
FM2	900	729	90	180	135	234.9	26.1	2.61	1.82
FM3									2.73
FM5									4.55

Following the Chinese standard mixing method for fiber-reinforced concrete (CECS 13:2009) [30], the traditional raw materials (excluding SFMs) were weighed according to the volume of cubic molds with a side length of 150 mm and mixed in a blender for 120 s. Water as the key component of the hydration reaction was then poured in and the mixing continued for 60 s. SFMs were subsequently scattered on the mixture's surface and evenly incorporated into the mortar with continuous mixing for another 60 s. To ensure the removal of bubbles generated during the mixing and pouring process, the flowing mortar was molded into a cube and placed on a vibrating table. To prevent the SFMs from floating on the upper mortar layer, the vibration time was limited to 30 s. Afterward, the cubic molds were cocooned with plastic wrap to avoid excess moisture loss and stored for 24 h in an air-conditioned chamber at 22 °C. Then, the mortar was demolded and transferred to a curing box with a moisture level of over 95% and a temperature of 22 °C [31]. After 28 days of curing, cylinders with a diameter of 48 mm were drilled out from the cured mortar blocks and cut into 24 mm thick cylinders. Following the dynamic test method for rock materials suggested by the International Society for Rock Mechanics and Rock Engineering (ISRM) [32,33], the cylinders were polished on both sides to a straightness of  $\pm 0.02$  mm and a roughness of 0.5% over the full thickness [33]. The prepared specimens were air-dried before testing, as depicted in Figure 1.



**Figure 1.** Specimens prepared for tests.

### 2.2. P-Wave Velocity Test

The P-wave velocity test as a non-destructive testing technology for concrete was employed to examine the interior integrity of the specimens [34,35]. The test apparatus consists of a pulse generator, an oscilloscope and two piezoelectric transducers. The two transducers connected to the signal transmitting and receiving ports are mounted on opposite sides of the specimen. To ensure efficient contact and wave transmission, vacuum grease was applied between the transducers and the specimen ends. Throughout the measurement process, an electrical signal was converted into a pressure pulse by one piezoelectric transducer and was then converted back by another. The time when the electrical signal was generated and received again was recorded by the oscilloscope, representing the wave propagation time in the specimen. The P-wave velocity was determined by calculating the ratio of the propagation length and time based on the thickness of each disc. The wave velocity of each sample was taken as the average value of the results obtained by placing the specimen in front and back. Three discs from the same position of the cubic mortar in each group of specimens were selected, and the average of their measurement results was taken as representative of the group.

### 2.3. Split Hopkinson Pressure Bar (SHPB) System

The SHPB system suggested by ISRM as a standard facility for determining the dynamic properties of rock-like materials could realize loading conditions with medium and high loading rates [33,36]. As illustrated in Figure 2, the striker driven by the pressurized air impacts the incident bar at a certain velocity, generating a stress wave that propagates through the bars and the specimen. The acoustic impedance of the bars and the specimen differs, resulting in wave reflection at the bar–specimen interface.

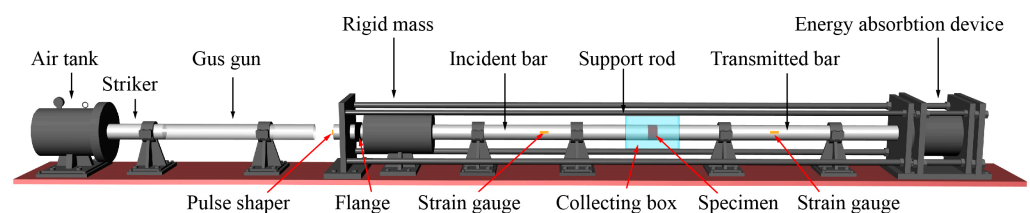


**Figure 2.** SHPB system with momentum trap and pulse shaping techniques.

According to the suggested method proposed by ISRM for determining the dynamic uniaxial compressive strength of rock materials with SHPB, the dynamic stress and strain of the specimen could be determined as [33]

$$\sigma = \frac{F_1 + F_2}{2} = \frac{AE}{2A_s} (\varepsilon_i + \varepsilon_r + \varepsilon_t), \quad (1)$$

$$\varepsilon = \frac{C_0}{l_0} \int_0^t (\varepsilon_i + \varepsilon_r + \varepsilon_t) d\tau, \quad (2)$$

where  $F_1 = EA(\varepsilon_i + \varepsilon_r)$  and  $F_2 = EA\varepsilon_t$  are the dynamic force subjected to the incident and transmitted ends of the specimen.  $E$  is the Young's modulus and  $A$  is the cross-sectional area of the bars;  $A_s$  is the cross-sectional area of the specimen;  $\varepsilon_i$ ,  $\varepsilon_r$  and  $\varepsilon_t$  are the strain histories associated with the incident, reflected and transmitted stress waves, respectively. It can be inferred that the force balance ( $F_1 = F_2$ ) indicates the stress equilibrium was achieved across the specimen, which verifies the effectiveness of the experiment. Therefore, the pulse shaping technique was adopted to slow down the rising speed of the incident stress wave, which left sufficient time for wave propagation and prevented local breakage caused by abrupt increases in stress [37]. As shown in Figure 2, a C1100 copper disc was attached to the impact end of the incident bar as a pulse shaper [38]. Figure 3 illustrates the resulting ramp pulse and the stress equilibrium indicated by the coincidence of transmitted stress and the sum of incident stress and reflected stress. The dynamic uniaxial compressive strength was determined as the peak value of the stress–time curve, where the slope of the rising edge was then defined as the loading rate. By adjusting the air pressure and the shaper size, the loading rate could be roughly controlled [26,33].

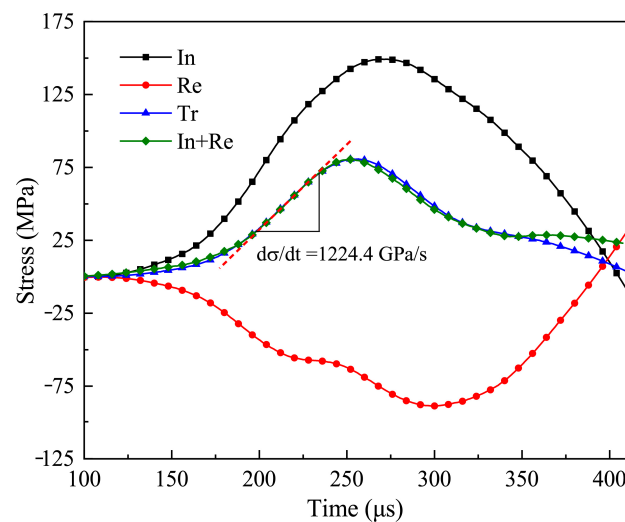


**Figure 3.** Dynamic stress balance and definition of the loading rate.

For subsequent fragmentation analysis, the momentum trap technology was additionally applied. As illustrated in Figure 2, the rigid mass and flange were, respectively, sleeved and fixed to the incident bar, leaving a gap between them. With this technique, the second wave generated at the impact end of reflection was transformed into a tensile wave after the passage of the first compression pulse [36,37]. The gap between the flange plate and the mass was set to the displacement of the impact end of the incident bar due to the incident pulse as Equation (3):

$$d = C \int_0^T \varepsilon_i(t) d\tau \quad (3)$$

where  $C$  is the one-dimensional P-wave velocity of the bar;  $T$  is the duration of the incident pulse; and  $\tau$  is the time integral variable [36].

#### 2.4. Energy Dissipation Analysis

In accordance with the law of energy conservation, the consumed energy in the loading process can be determined as the energy difference before and after the stress wave acts on the specimen:

$$\Delta W = W_i - W_r - W_t \quad (4)$$

$$W(t) = AEC \int_0^t \varepsilon^2(t) d\tau \quad (5)$$

where  $W$  is the energy of the stress wave and can be calculated as Equation (5);  $W_i$ ,  $W_r$  and  $W_t$  are the energy associated with the incident, reflected and transmitted stress waves, respectively. Previous studies found that the dissipated energy of the specimen accounts for about 95% of the energy input to the specimen [39]. Therefore, the consumed energy  $\Delta W$  was used to approximate the dissipated energy. To minimize the interference caused by geometric factors of the specimen, the dissipated energy density is defined here as the ratio of the total energy dissipated to the volume.

### 2.5. Sieve Analysis

Sieve analysis was conducted on the broken specimens to quantitatively evaluate the fragmentation, which can be informative for the study of the damage evolution of the material, and the dismantling of the structure after service [40]. Following the standard test method for sieve analysis of fine and coarse aggregates recommended by the American Society for Testing and Materials (ASTM) [41], a pile of sieves with aperture sizes of 40 mm, 20 mm, 10 mm, 5 mm, 2 mm, 1 mm, 0.5 mm, 0.25 mm and 0.075 mm was used. The sieves were stacked in descending order of their aperture size and a collector box was placed at the bottom. After shaking the stack manually for 5 min, the fragments of different sizes remained on the sieve with a smaller aperture and the retained mass in each sieve was measured by an electronic scale with an accuracy of 0.01 g. The fragmentation size distribution could then be summarized based on the weighing results.

## 3. Results

### 3.1. P-Wave Velocity

The P-wave velocity of specimens of different SFM content groups is shown in Figure 4. As can be seen, the P-wave velocity does not exhibit a monotonic change with mask content. It decreases when the SFM content is 0.2% and 0.5%, while reaching its maximum at 0.3%. However, it should be noted that the P-wave velocity shows a significant increase across all mixing designs when compared to the control group. Specifically, the P-wave velocity increases by 8.03%, 5.33%, 12.16% and 6.85% with the increase in SFM content. A general improving effect of mask inclusion was also found in the study of SFM-reinforced concrete [7,21]. Previous studies have proven that the propagation velocity of the P-wave in mortar and concrete is positively related to their static mechanical properties, such as strength and Young's modules. This improvement in these properties was attributed to the improved quality [42]. Furthermore, microscopic observations of the mask-incorporated concrete by a scanning electron microscope (SEM) revealed that the mask fibers and cement matrix exhibit a strong interface connection [21]. Therefore, it can be inferred that the SFM inclusion results in a limited amount of microcracks in the specimen [43].

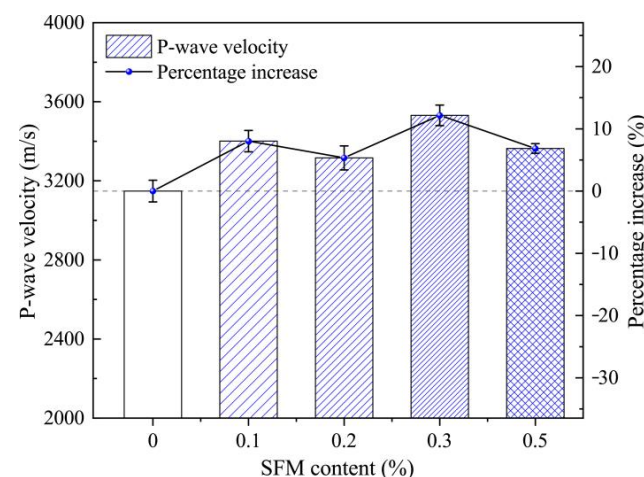
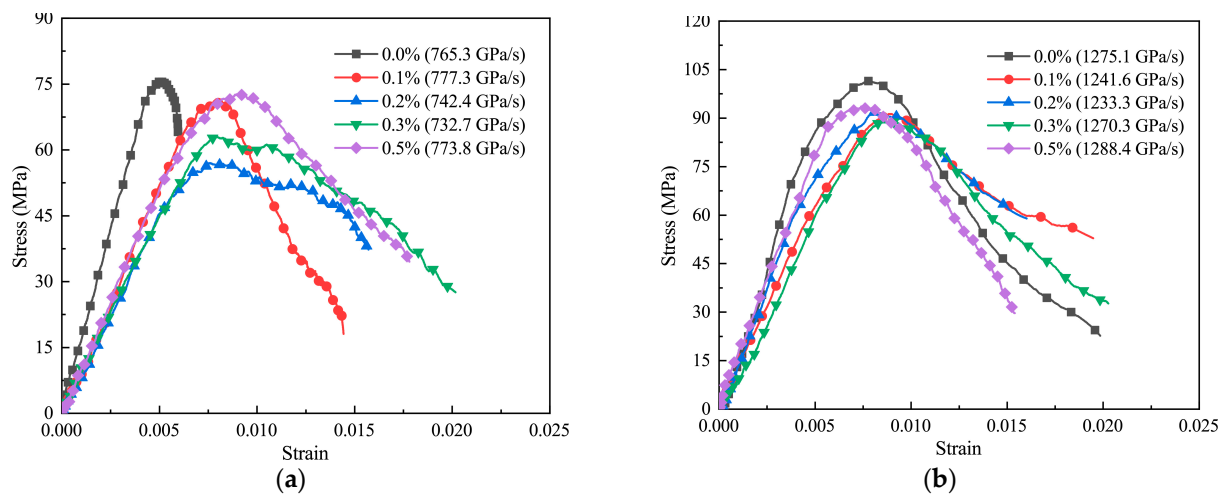


Figure 4. P-wave velocity of the mortars with different SFM contents.

### 3.2. Dynamic Stress–Strain Curves and Strength Characteristics

After the stress equilibrium is verified, the dynamic stress–strain curve of the specimen can be calculated and plotted according to Equations (1) and (2). Figure 5 demonstrates the dynamic stress–strain curves for two sets of mortars with SFMs incorporated (SFM–mortar) at similar loading rates (about 750 GPa/s and 1250 GPa/s). At the lower loading rate, the dynamic uniaxial compressive strength (DUCS) of mortars is decreased across all SFM-incorporating designs. On the contrary, the peak strain corresponding to the peak stress of the SFM–mortar tends to increase. Thus, the area obtained from the integration of the stress–strain curve is larger and the specimen deforms more before the stress peaks, implying that the SFM–mortar may accumulate more energy. In addition, the elastic modulus of SFM–mortar is much lower. The SFM incorporation increases the deformation capacity under dynamic loading. The strength reduction of SFM–mortar is also found at the higher loading rate. However, changes in the elastic modulus and peak strain are inconspicuous. The effect of SFMs on these two mechanical parameters does not follow a clear pattern with the content.



**Figure 5.** Dynamic stress–strain curves at lower and higher loading rates: (a) about 750 GPa/s; (b) about 1250 GPa/s.

The dynamic uniaxial compressive strength (DUCS) of specimens with varying SFM contents and different loading rates is depicted in Figure 6. It is observed that the DUCS of both plain mortar and mortar with SFM incorporated (SFM–mortar) is rate-dependent, displaying an approximately linear growth with the loading rate. However, the fitting curves of SFM–mortar consistently fall below those of the control group, indicating a reduced compressive strength of SFM–mortar within the loading rate range studied. This contrasts with the results of previous quasi-static uniaxial compressive tests, where the strength exhibited a consistent improvement [7]. To facilitate a visual comparison of the DUCS among mortars with different SFM contents, the test results with loading rates around 900 GPa/s and 1200 GPa/s (where the loading rate error of the surrounding data points is strictly controlled within 50 GPa/s) were selected and are graphically illustrated in Figure 7. It can be observed that the DUCS follows a trend of an initial decrease followed by an increase. The compressive strength reaches its minimum when the SFM volume content is 0.2% at both loading rates. It is noteworthy that the DUCS decreased for all SFM–mortar groups, with a proportion range of decline of 0.49% to 9.88% and 2.83% to 13.52% at loading rates of 900 GPa/s and 1200 GPa/s, respectively. Combined with the results of quasi-static experiments on mortars with similar SFM contents, it can be observed that the effect of SFMs on the quasi-static and dynamic compressive properties of mortars is different [24]. The loss of uniaxial compressive strength increases with the loading rate.

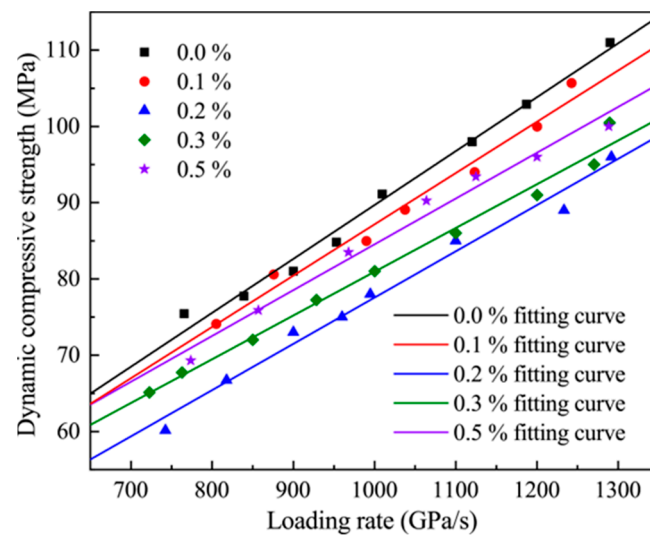


Figure 6. Dynamic uniaxial compression strength of mortar with different SFM contents.

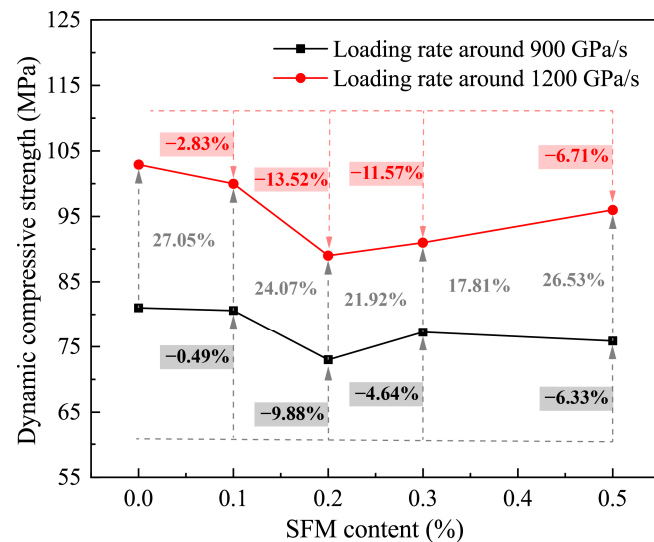


Figure 7. Comparison of dynamic uniaxial compression strength of mortars at given loading rates.

### 3.3. Dissipated Energy Density

The dissipated energy refers to the energy consumed by the specimen in the loading process and serves as an evaluation indicator of the specimen's energy absorption capacity. The calculated dissipated energy density of specimens with varying SFM inclusion is plotted against the loading rate in Figure 8. It is evident that the dissipated energy density rises almost linearly with the loading rate. Unlike DUCS, the dissipated energy density of all SFM–mortars is significantly increased at lower loading rates. Nevertheless, the fitting curve gradually approaches with the increase in the loading rate, indicating that the energy absorption capacity of mortar with varied SFM content changes little when the loading rate reaches about 1300 GPa/s. To further illustrate this phenomenon, the test results with loading rates around 850 GPa/s and 1250 GPa/s were selected under the same standard as the DUCS comparison and are shown in Figure 9. It is observed that the dissipated energy density exhibits a similar trend with the P-wave velocity (Figure 4) at the loading rate of 850 GPa/s. In other words, both the dissipated energy density and P-wave velocity reach the minimum value when the SFM content is 0.2% and the maximum when the SFM content is 0.3%. The dissipated energy density generally improves with mask inclusion, with an improvement range of 109.44% to 200.99%. However, the change in dissipated energy density at the loading rate of 1250 GPa/s is within 5.03%. The influence of SFMs

on the energy absorption capacity becomes gradually insignificant with the increasing loading rate.

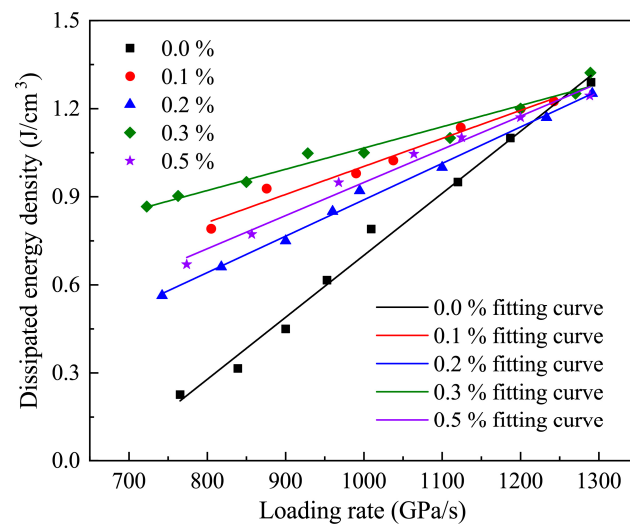


Figure 8. Dissipated energy density of mortars at various loading rates.

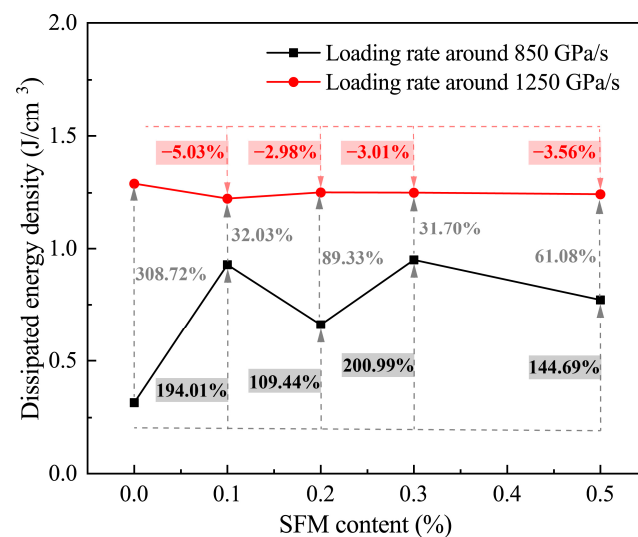
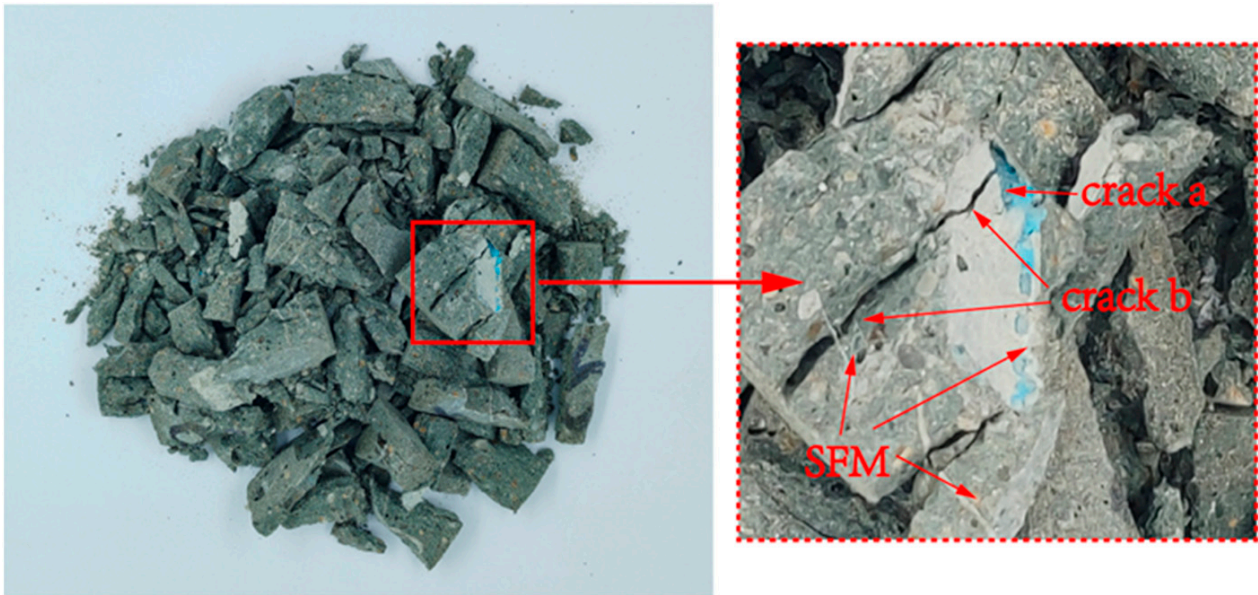


Figure 9. Comparison of the dissipated energy density of mortars at given loading rates.

### 3.4. Specimen Fragmentation

In the dynamic loading process, the specimen was broken, and the fragments were collected by the collecting box. The typical crushed morphology of the specimen after dynamic compression is depicted in Figure 10. It can be recognized that the blue or white SFM exists in a three-dimensional form within the mortar. As seen in the local magnified view, the SFM is strongly bonded to the cement matrix. The bond between the SFM and the mortar was locally destroyed by cracks in different forms: (1) the SFM would separate from the mortar on one side when the crack developed parallel to the SFM strip surface (crack a); (2) the mask would tear, with the SFM strip edge exposed when the crack was perpendicular to the surface (crack b).



**Figure 10.** Crushed morphology of the specimen.

The fragmentation size distribution of the specimens was obtained from the sieve test. The comparison results under the loading rates of 900 GPa/s and 1200 GPa/s are summarized in Figure 11. It is observed that the curves of SFM–mortar grow faster towards the maximum, indicating that SFM–mortar has fewer large pieces after being loaded. Moreover, there were more fragments of small sizes at 1200 GPa/s and the curves in Figure 11b reach 100% earlier. This shows that the increase in the loading rate led to more severe specimen damage [39]. However, the stacking order of the curves changes under different loading rates. The mortar containing 0.2% SFM exhibited the most severe damage at the loading rate of 900 GPa/s, while this comparative disadvantage was less significant at 1200 GPa/s. This suggests that the influence of SFMs on the fragmentation degree of the specimen varies with the loading rates.

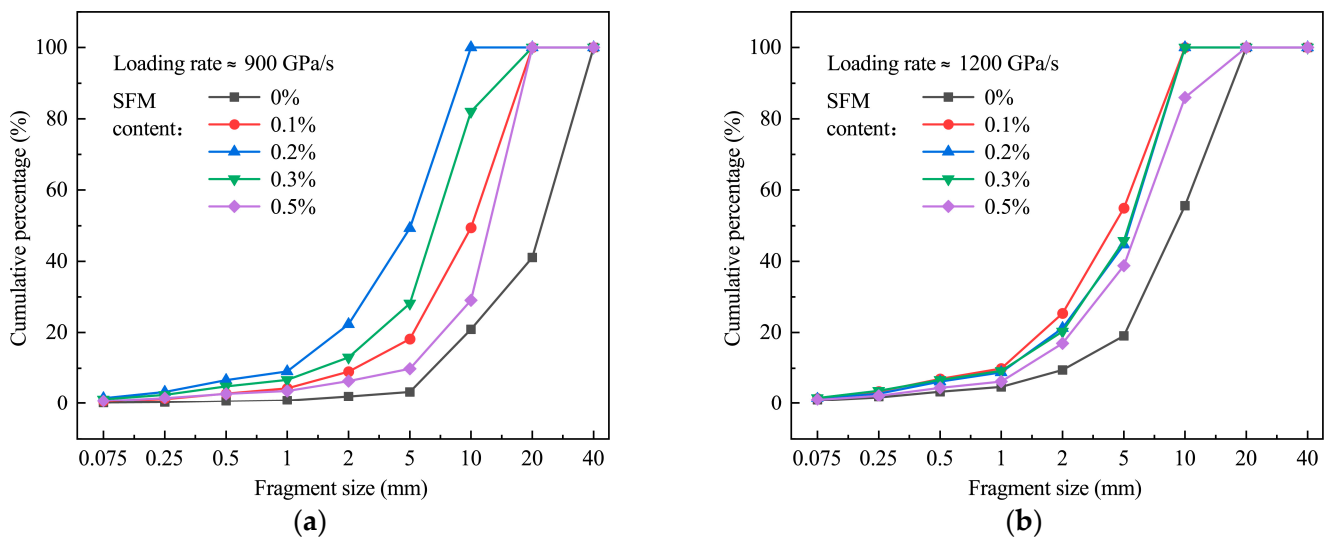


**Figure 11.** Fragmentation size distribution of specimens under given loading rates: (a) 900 GPa/s; (b) 1200 GPa/s.

### 3.5. Damage Constitutive Model Based on the Modified Weibull Distribution and Lemaitre Principle

The accumulation of internal damage is the result of the destruction of the material. Therefore, the evolution of damage is inevitably accompanied by the dissipation of energy. This is demonstrated by the same trend in the energy consumed by the mortar specimens during dynamic loading (illustrated in Figure 8) as well as in the degree of specimen fragmentation (statistically presented in Figure 11). Therefore, the effects of mask inclusion and changes in material properties are reflected in the energy consumption of the specimen deformation and destruction process [44]. It is possible to characterize the dynamic response of SFM–mortars in terms of material damage and energy dissipation.

The strain constitutive relationship of damaged materials can be derived from the constitutive equation of non-destructive materials by using the assumption of strain equivalence or strain energy proposed by Lemaitre [45]. Specially, the strain of the nominal stress acting on a damaged material is equal to the strain of the effective stress acting on an undamaged material, introducing the damage variable  $D$ , as Equation (6) expresses [46]:

$$\varepsilon = \frac{\sigma^*}{E(1-D)} = \frac{\sigma}{E} \quad (6)$$

where  $\sigma^*$  is the nominal stress;  $\sigma$  is the effective stress;  $D$  is the damage variable; and  $E$  is the modulus of elasticity.

Assuming that the probability of the microelement failure of mortar and the dissipated energy  $W$  satisfy a Weibull probability density relationship, the damage parameter can be calculated according to the simplified two-parameter Weibull distribution form [47]:

$$D = \frac{N}{N_t} = \frac{N_t(1 - \exp(-\frac{V}{V_0}(\frac{W}{W_0})^B))}{N_t} = (1 - \exp(-\frac{V}{V_0}(\frac{W}{W_0})^B)) \quad (7)$$

where  $N$  is the damage microelement number;  $N_t$  is the total microelement number;  $V$  is the specimen volume;  $V_0$  is the reference volume;  $W$  is the dissipated energy and  $W_0$  is the reference energy; and  $B$  is the Weibull parameter that can be obtained by the inversion of the experimental data. Due to the complex effects of SFMs and the availability of the parameters, a further simplification of Equation (7) was conducted. Specially,  $A = V/V_0$  as taken as another Weibull parameter and  $W_0$  was taken as the test value of the energy consumed by the specimen in the experiment [47].

Combining Equations (6) and (7), the stress–strain principal relationship under dynamic compression can be described as

$$\sigma = E\varepsilon \exp\left(-A\left(\frac{W(\varepsilon)}{\Delta W}\right)^B\right) \quad (8)$$

where  $W(\varepsilon)$  is the energy consumed at the current strain and can be calculated according to Equations (2), (4) and (5).

To verify whether the constitutive model can describe the dynamic stress–strain relation of SFM–mortars at different loading rates or not, the theoretical stress–strain curves of the newly constitutive model were compared with the experimental results as shown in Figure 12. For mortar specimens with different SFM contents, the stress–strain curves from Equation (8) are in good agreement with those curves obtained from experiments, indicating the model not only can fully illustrate the relation between strength, strain and loading rate, but can also capture the variation in the mechanical properties of mask incorporation.

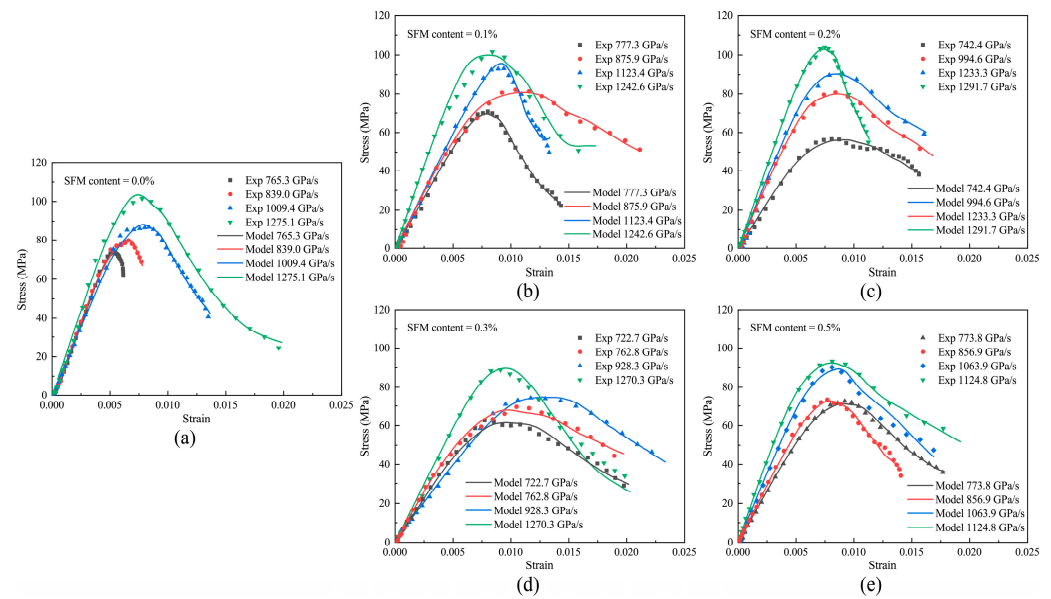


**Figure 12.** Comparison between experimental results and model curves: (a) 0%; (b) 0.1%; (c) 0.2%; (d) 0.3%; (e) 0.5%.

#### 4. Discussion

The loading rate is a crucial variable in dynamic tests. The results indicate that the DUCS, dissipated energy density and specimen fragmentation degree are all dependent on the loading rate. The improvement could be attributed to dynamic transient loading, resulting in insufficient time for crack propagation [26]. Additionally, the SFM–mortar can be understood as if the two parts, the cement matrix and the SFM, were bonded together (for the plain mortar, only the cement matrix). The strength is enhanced by more of the matrix participating in the force, leading to the generation of more microcracks inside the specimen during loading and, ultimately, more severe breakage [39]. The energy consumed to generate new surfaces and convert into other forms increases, as reflected in the growth of the dissipated energy density [48,49]. Meanwhile, greater stress causes more local weakening and failure, resulting in fewer large pieces remaining, as indicated in the fragment grading curve (Figure 11).

Furthermore, the P-wave velocity, as a macroscopic index characterizing the internal structure of the specimen, increases when the propagation media are dense and uniform [50,51]. The SFM acting as a dopant is strongly bonded to the cement matrix while limiting the formation of microcracks, as observed in the local crushed morphology of specimens (Figure 10). The mortar solids are connected by the SFM, resulting in the improved integrity and compactness of the specimen. This compact effect means more energy is needed to fracture the specimen [39]. Therefore, the dissipated energy density increases and exhibits a similar trend to the P-wave velocity. However, the interfacial transition zone (ITZ) between the mask and the cement matrix cannot be eliminated. The existence and concentrated distribution of ITZs near the SFM pieces bring about structural discontinuity, which can be regarded as the internal defect of dense mortar material [26,52]. The slight drop in the P-wave velocity at 0.2% SFM content could be attributed to the accumulation of these internal defects. Additionally, the incorporated SFM fibers were more likely interwoven into clusters with increased content, and more porous structures developed inside the specimen [53]. This led to a decrease in mortar quality at 0.5% SFM content [7,54].

The effects of SFMs in the cement matrix can be summarized based on previous studies on the reinforced mechanism of fiber-reinforced concrete, as illustrated in Figure 13. Depending on the deformation of the SFM and the relative movement between the SFM and the cement matrix, the mask strips may exhibit rupturing, pullout, bridging or debonding to the cement matrix under load [55]. When cracks initiate and develop, the SFM bridges

the split parts of the specimens and facilitates stress transfer from the matrix to the SFM [54]. The SFM may break, be pulled out or be elongated, as defined by types (a), (b) and (c), respectively. Cracks in such cases develop perpendicularly or at an incline to the SFM (crack a in Figure 10). These SFMs contribute to the improvement of strength and maintain integrity, as reflected in the increasing trend of the DUCS in Figure 7. However, SFM strips have larger dimensions in two directions. Cracks may develop along the SFM surface in multiple directions due to the presence of ITZ, causing the SFM to play the role of debonding (type (d) in Figure 13) and exposing the mask, as shown in Figure 10 (crack b). Meanwhile, the debonding of the SFM with the mortar gives more paths for cracks to develop. Therefore, the specimen is severely broken by the secondary cracks and the fragmentation degree of the specimen is increased by the multiple effects of the SFM.

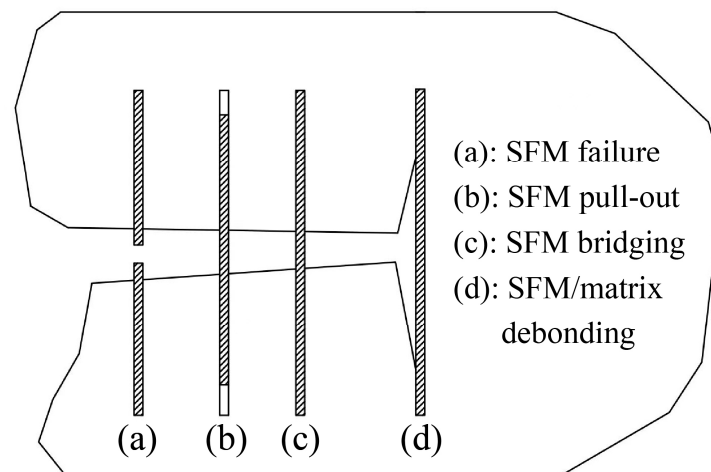


**Figure 13.** Effects of the SFM in a cement matrix at the crack tip.

When the specimen is stressed, cracks are first initiated in the weakened area inside the specimen and eventually cause different forms of destruction of SFM–cement matrix bonding. Especially under high-speed loading, the cracks around ITZs develop more sufficiently. The weakening effect (type (d)) caused by the SFM size is more significant. The weak interfacial area between the SFM and cement matrix, together with more cracks, contributes to the increasing DUCS reduction with the loading rate [56]. The bridging effect of the SFM increases with the increasing content, which leads to a turnaround of the DUCS at 0.2% SFM content. However, the increase in content also leads to an increase in the defects inside a specimen, so the DUCS is decreased for all mixing designs compared to the plain mortars. In addition, there is no obvious regularity in the degree of fragmentation of the specimens.

As an essential feature of the loading processes in dynamic experiments, energy dissipation reflects the inherent properties of the material, which are further illustrated by the applicability of statistical damage constitutive models based on energy calculations. The enhancement of the energy absorption capacity primarily stems from the improved quality of mortar [57]. Additionally, additional energy is consumed due to SFM deformation or friction with the matrix as more energy is consumed to fracture the specimen and generate new surfaces [57,58]. During this process, the damage gradually develops. However, fracture energy is the main form of energy consumption. The proportion of energy consumed by the SFM is small and could be negligible with the increasing fragmentation degree [57]. With the loading rate increasing, the difference in the specimen fragmentation degree decreases gradually, as Figure 11 reveals. Therefore, the influence of the SFM on the energy absorption capacity is less significant at higher loading rates.

## 5. Conclusions

Dynamic uniaxial compression tests of mortar with four contents of SFM inclusion and plain mortar were conducted with an SHPB system, and the integrity reflected by the P-wave velocity, dynamic response and energy absorption capacity were comparatively analyzed. The P-wave velocity of the mortar increased across all mask-mixing designs, and the enhancing effect on the overall quality can be attributed to the limitation of microcracks. On the one hand, the elastic modulus and peak strain of mortars were, respectively, decreased and increased with the SFM content, indicating the weakening effect of mask inclusion on the resistance to deformation. On the other hand, the increase in the loading rate enhanced the elastic modulus of the mortar, reducing the weakening effect of the SFM. The dynamic uniaxial compressive strength, which has a linear rate-dependency, was generally decreased by the internal defect caused by SFM inclusion and dropped to the minimum at 0.2% SFM content. Moreover, the weakening effect of the SFM on the dynamic uniaxial compressive strength increased with the increasing loading rate, which could be attributed to the facilitating effect of the specially shaped SFM on the development of cracks in the specimens and the destructive effect on the homogeneity of the mortar material. However, the mortar with mask inclusion possessed higher energy absorption capacity, which exhibited a similar trend with the P-wave velocity. The enhancement of the energy absorption capacity of the mortar was gradually negligible as the loading rate increased. At the same time, the degree of fragmentation of the specimens gradually increased, and the difference between mortars with various SFM contents did not show a clear trend. Combining the complex effects of the loading rate and SFM inclusion, a form of constitutive model based on Weibull distribution and the Lemaitre principle is proposed. The applicability of the model was verified by calibrating the parameters based on experimental data. The results show that the developed model can reproduce the relationship between the stress, strain, loading rate and SFM content well.

The structure and shape of the mask have specific characteristics that do not allow it to have exactly the same action as polypropylene fibers. However, the mechanism of the masks does not go beyond the mechanism of fiber action on concrete-like materials, and from this point of view, the results of the present study are not in conflict with previous studies. For building materials containing SFMs, caution should be exercised when applying them in areas that may be subject to dynamic compressive loads. The potential benefits of SFMs in terms of integrity and static strength need to be balanced against the potential risks associated with their use in transient loading environments. As such, careful consideration should be given to the specific context in which material with mask inclusion is being used, and appropriate design and testing protocols should be followed to ensure safety and reliability.

**Author Contributions:** Conceptualization, Q.N. and B.W.; Data curation, X.D. and L.C.; Formal analysis, Z.W. and X.D.; Funding acquisition, Q.N.; Investigation, Z.W.; Methodology, Q.N. and Z.W.; Resources, Q.N.; Supervision, B.W.; Writing—original draft, L.C.; Writing—review and editing, Z.W. All authors have read and agreed to the published version of the manuscript.

**Funding:** This research was funded by the Research Project of the Teaching Guidance Sub-Committee for Engineering Management and Engineering Cost Majors under the Ministry of Education of China (CMPC202132), the Construction Science and Technology Plan Project of Hubei province (2020-30), and the Teaching and Research Project of Hubei University of Education (X2018094).

**Data Availability Statement:** The raw data supporting the conclusions of this article will be made available by the authors on request.

**Conflicts of Interest:** The authors declare no conflicts of interest.

## References

1. Haji, J.Y.; Subramaniam, A.; Kumar, P.; Ramanathan, K.; Rajamani, A. State of personal protective equipment practice in indian intensive care units amidst COVID-19 pandemic: A nationwide survey. *Indian J. Crit. Care Med.* **2020**, *24*, 809–816. [[CrossRef](#)] [[PubMed](#)]
2. Chua, M.H.; Cheng, W.R.; Goh, S.S.; Kong, J.H.; Li, B.; Lim, J.Y.C.; Mao, L.; Wang, S.X.; Xue, K.; Yang, L.; et al. Face masks in the new COVID-19 normal: Materials, testing, and perspectives. *Research* **2020**, *2020*, 7286735. [[CrossRef](#)] [[PubMed](#)]
3. Prata, J.C.; Silva, A.L.P.; Walker, T.R.; Duarte, A.C.; Rocha-Santos, T. COVID-19 pandemic repercussions on the use and management of plastics. *Environ. Sci. Technol.* **2020**, *54*, 7760–7765. [[CrossRef](#)] [[PubMed](#)]
4. Park, Y.; Bae, H.; Park, H.; Park, J.; Hong, J.; Kim, Y. The Unseen Threat: Microplastic Emissions from Face Masks and Limited Public Awareness. *Korean J. Chem. Eng.* **2024**, *41*, 237–247. [[CrossRef](#)]
5. Aragaw, T.A. Surgical face masks as a potential source for microplastic pollution in the COVID-19 scenario. *Mar. Pollut. Bull.* **2020**, *159*, 111517. [[CrossRef](#)] [[PubMed](#)]
6. Idrees, M.; Akbar, A.; Mohamed, A.M.; Fathi, D.; Saeed, F. Recycling of waste facial masks as a construction material, a step towards sustainability. *Materials* **2022**, *15*, 1810. [[CrossRef](#)] [[PubMed](#)]
7. Kilmartin-Lynch, S.; Saberian, M.; Li, J.; Roychand, R.; Zhang, G.M. Preliminary evaluation of the feasibility of using polypropylene fibres from COVID-19 single-use face masks to improve the mechanical properties of concrete. *J. Cleaner Prod.* **2021**, *296*, 126460. [[CrossRef](#)] [[PubMed](#)]
8. Chen, X.C.; Chen, X.F.; Liu, Q.; Zhao, Q.C.; Xiong, X.; Wu, C.X. Used disposable face masks are significant sources of microplastics to environment. *Environ. Pollut.* **2021**, *285*, 117485. [[CrossRef](#)] [[PubMed](#)]
9. Fadare, O.O.; Okoffo, E.D. COVID-19 face masks: A potential source of microplastic fibers in the environment. *Sci. Total Environ.* **2020**, *737*, 140279. [[CrossRef](#)]
10. Sullivan, G.L.; Delgado-Gallardo, J.; Watson, T.M.; Sarp, S. An investigation into the leaching of micro and nano particles and chemical pollutants from disposable face masks-linked to the COVID-19 pandemic. *Water Res.* **2021**, *196*, 117033. [[CrossRef](#)] [[PubMed](#)]
11. Hu, X.; Lin, Z.D. Transforming waste polypropylene face masks into S-doped porous carbon as the cathode electrode for supercapacitors. *Ionics* **2021**, *27*, 2169–2179. [[CrossRef](#)] [[PubMed](#)]
12. Fox, J.A.; Stacey, N.T. Process targeting: An energy based comparison of waste plastic processing technologies. *Energy* **2019**, *170*, 273–283. [[CrossRef](#)]
13. Awoyera, P.O.; Effiong, J.U.; Olalusi, O.B.; Arunachalam, K.P.; de Azevedo, A.R.G.; Martinelli, F.R.B.; Monteiro, S.N. Experimental findings and validation on torsional behaviour of fibre-reinforced concrete beams: A review. *Polymers* **2022**, *14*, 1171. [[CrossRef](#)] [[PubMed](#)]
14. Dey, D.; Srinivas, D.; Panda, B.; Suraneni, P.; Sitharam, T.G. Use of industrial waste materials for 3D printing of sustainable concrete: A review. *J. Clean. Prod.* **2022**, *340*, 130749. [[CrossRef](#)]
15. Gong, J.H.; Ma, Y.W.; Fu, J.Y.; Hu, J.; Ouyang, X.W.; Zhang, Z.H.; Wang, H. Utilization of fibers in ultra-high performance concrete: A review. *Compos. Part B-Eng.* **2022**, *241*, 109995. [[CrossRef](#)]
16. Wang, W.; Wei, W.Y.; Gao, S.; Chen, G.M.; Yuan, J.; Li, Y. Agricultural and aquaculture wastes as concrete components: A review. *Front. Mater.* **2021**, *8*, 762568. [[CrossRef](#)]
17. Guo, H.; Tao, J.L.; Chen, Y.; Li, D.; Jia, B.; Zhai, Y. Effect of steel and polypropylene fibers on the quasi-static and dynamic splitting tensile properties of high-strength concrete. *Constr. Build. Mater.* **2019**, *224*, 504–514. [[CrossRef](#)]
18. Li, F.R.; Chen, G.X.; Xu, G.Z.; Wu, Y.Y. An experimental study on the compressive dynamic performance of polypropylene fiber reinforced concrete for retaining structure under automobile collision magnitude. *Adv. Civ. Eng.* **2020**, *2020*, 8826006. [[CrossRef](#)]
19. Liu, J.L.; Jia, Y.M.; Wang, J. Experimental study on mechanical and durability properties of glass and polypropylene fiber reinforced concrete. *Fibers Polym.* **2019**, *20*, 1900–1908. [[CrossRef](#)]
20. Saberian, M.; Li, J.; Kilmartin-Lynch, S.; Boroujeni, M. Repurposing of COVID-19 single-use face masks for pavements base/subbase. *Sci. Total Environ.* **2021**, *769*, 145527. [[CrossRef](#)] [[PubMed](#)]
21. Abd El Aal, A.; Abdullah, G.M.S.; Qadri, S.M.T.; Abotalib, A.Z.; Othman, A. Advances on concrete strength properties after adding polypropylene fibers from health personal protective equipment (PPE) of COVID-19: Implication on waste management and sustainable environment. *Phys. Chem. Earth* **2022**, *128*, 103260. [[CrossRef](#)] [[PubMed](#)]
22. Paul, S.C.; Santo, M.A.H.; Nahid, S.A.; Majumder, A.R.; Al Mamun, M.F.; Basit, M.A.; Babafemi, A.J. Potential Use of COVID-19 Surgical Masks and Polyethylene Plastics in Developing Sustainable Concrete. *J. Compos. Sci.* **2023**, *7*, 402. [[CrossRef](#)]
23. Maloba, J.W.; Kiambigi, J.M.; Kabubo, C.K. Reutilizing Single-Use Surgical Face Masks to Improve the Mechanical Properties of Concrete: A Feasibility Study. *Eng. Technol. Appl. Sci. Res.* **2023**, *13*, 10511–10516. [[CrossRef](#)]
24. Ajam, L.; Trabelsi, A.; Kammoun, Z. Valorisation of face mask waste in mortar. *Innov. Infrastruct. Solut.* **2022**, *7*, 130. [[CrossRef](#)]
25. Avudaippan, S.; Cendoya, P.; Arunachalam, K.P.; Maureira-Carsalade, N.; Canales, C.; Amran, M.; Parra, P.F. Innovative Use of Single-Use Face Mask Fibers for the Production of a Sustainable Cement Mortar. *J. Compos. Sci.* **2023**, *7*, 214. [[CrossRef](#)]
26. Li, X.; Xia, K.W.; Yao, W.; Xu, Y. Investigation on the dynamic tensile behaviour of rubberized mortar using the Brazilian disc method. *Theor. Appl. Fract. Mech.* **2022**, *119*, 103339. [[CrossRef](#)]
27. Abna, A.; Mazloom, M. Flexural properties of fiber reinforced concrete containing silica fume and nano-silica. *Mater. Lett.* **2022**, *316*, 132003. [[CrossRef](#)]

28. Garg, R.; Garg, R. Performance evaluation of polypropylene fiber waste reinforced concrete in presence of silica fume. In Proceedings of the International Conference on Advanced Materials Behavior and Characterization (ICAMBC), Chennai, India, 24–26 April 2021; pp. 809–816.
29. Xiang, Y.; Song, Q.F.; Gu, W.Z. Decontamination of surgical face masks and N95 respirators by dry heat pasteurization for one hour at 70 degrees C. *Am. J. Infect. Control* **2020**, *48*, 880–882. [[CrossRef](#)] [[PubMed](#)]
30. CECS 13; Standard Test Methods for Fiber Reinforced Concrete. China Construction Engineering Association: Beijing, China, 2009.
31. Xu, H.Y.; Shao, Z.M.; Wang, Z.J.; Cai, L.B.; Li, Z.; Jin, H.S.; Chen, T.W. Experimental study on mechanical properties of fiber reinforced concrete: Effect of cellulose fiber, polyvinyl alcohol fiber and polyolefin fiber. *Constr. Build. Mater.* **2020**, *261*, 120610. [[CrossRef](#)]
32. Xia, K.; Yao, W. Dynamic rock tests using split Hopkinson (Kolsky) bar system—A review. *J. Rock Mech. Geotech. Eng.* **2015**, *7*, 27–59. [[CrossRef](#)]
33. Zhou, Y.X.; Xia, K.; Li, X.B.; Li, H.B.; Ma, G.W.; Zhao, J.; Zhou, Z.L.; Dai, F. Suggested methods for determining the dynamic strength parameters and mode-I fracture toughness of rock materials. *Int. J. Rock Mech. Min. Sci.* **2012**, *49*, 105–112. [[CrossRef](#)]
34. Demirboga, R.; Turkmen, I.; Karakoc, M.B. Relationship between ultrasonic velocity and compressive strength for high-volume mineral-admixed concrete. *Cem. Concr. Res.* **2004**, *34*, 2329–2336. [[CrossRef](#)]
35. Yao, W.; Xu, Y.; Wang, W.; Kanopolous, P. Dependence of dynamic tensile strength of Longyou sandstone on heat-treatment temperature and loading rate. *Rock Mech. Rock Eng.* **2015**, *49*, 3899–3915. [[CrossRef](#)]
36. Wang, S.; Xu, Y.; Xia, K.W.; Tong, T.Y. Dynamic fragmentation of microwave irradiated rock. *J. Rock Mech. Geotech. Eng.* **2021**, *13*, 300–310. [[CrossRef](#)]
37. Xia, K.; Nasser, M.H.B.; Mohanty, B.; Lu, F.; Chen, R.; Luo, S.N. Effects of microstructures on dynamic compression of Barre granite. *Int. J. Rock Mech. Min. Sci.* **2008**, *45*, 879–887. [[CrossRef](#)]
38. Xu, Y.; Yao, W.; Wang, S.; Xia, K.W. Investigation of the heat-treatment effect on rock fragmentation characteristics using the dynamic ball compression test. *Rock Mech. Rock Eng.* **2020**, *53*, 2095–2108. [[CrossRef](#)]
39. Wu, B.B.; Yang, L.; Mei, Y.; Sun, Y.H.; Liu, J.M.; Shen, J. Effects of Freeze-Thaw Cycling on Dynamic Compressive Strength and Energy Dissipation of Sandstone. *Minerals* **2022**, *12*, 1331. [[CrossRef](#)]
40. Ren, W.B.; Xu, J.Y. Fractal Characteristics of Concrete Fragmentation under Impact Loading. *J. Mater. Civ. Eng.* **2017**, *29*, 04016244. [[CrossRef](#)]
41. ASTM C136-06; Standard Test Method for Sieve Analysis of Fine and Coarse Aggregates. ASTM: West Conshohocken, PA, USA, 2006.
42. Yap, S.P.; Alengaram, U.J.; Jumaat, M.Z. Enhancement of mechanical properties in polypropylene- and nylon-fibre reinforced oil palm shell concrete. *Mater. Des.* **2013**, *49*, 1034–1041. [[CrossRef](#)]
43. Shen, D.J.; Liu, X.Z.; Zeng, X.; Zhao, X.G.; Jiang, G.Q. Effect of polypropylene plastic fibers length on cracking resistance of high performance concrete at early age. *Constr. Build. Mater.* **2020**, *244*, 117874. [[CrossRef](#)]
44. Peng, R.D.; Ju, Y.; Wang, J.G.; Xie, H.P.; Gao, F.; Mao, L.T. Energy Dissipation and Release During Coal Failure Under Conventional Triaxial Compression. *Rock Mech. Rock Eng.* **2015**, *48*, 509–526. [[CrossRef](#)]
45. Lemaitre, J. How to use damage mechanics. *Nucl. Eng. Des.* **1984**, *80*, 233–245. [[CrossRef](#)]
46. Ji, Y.C.; Wang, D.Y. Constitutive model of waste brick concrete based on Weibull strength theory. *Case Stud. Constr. Mater.* **2023**, *18*, e01738. [[CrossRef](#)]
47. Chen, X.D.; Wu, S.X.; Zhou, J.K. Compressive Strength of Concrete Cores with Different Lengths. *J. Mater. Civ. Eng.* **2014**, *26*, 04014027. [[CrossRef](#)]
48. Khazaei, C.; Hazzard, J.; Chalaturnyk, R. Damage quantification of intact rocks using acoustic emission energies recorded during uniaxial compression test and discrete element modeling. *Comput. Geotech.* **2015**, *67*, 94–102. [[CrossRef](#)]
49. Wang, F.; Wang, H.B.; Xu, Y.; Cheng, B.; Wang, Q.Q. Analysis of energy dissipation characteristics of damaged sandstone under impact load. *Shock Vib.* **2021**, *2021*, 4200452. [[CrossRef](#)]
50. Gul, R.; Demirboga, R.; Guvercin, T. Compressive strength and ultrasound pulse velocity of mineral admixed mortars. *Indian J. Eng. Mat. Sci.* **2006**, *13*, 18–24.
51. Li, X.; Wang, S.; Xu, Y.; Yao, W.; Xia, K.W.; Lu, G.M. Effect of microwave irradiation on dynamic mode-I fracture parameters of Barre granite. *Eng. Fract. Mech.* **2020**, *224*, 106748. [[CrossRef](#)]
52. Kilmartin-Lynch, S.; Roychand, R.; Saberian, M.; Li, J.; Zhang, G. Application of COVID-19 single-use shredded nitrile gloves in structural concrete: Case study from Australia. *Sci. Total Environ.* **2022**, *812*, 151423. [[CrossRef](#)]
53. Xu, Y.; Cui, T.; Wu, B.; Wang, Z.; Song, Y. Dynamic mode I fracture characteristics of jute fiber-reinforced rubber mortar. *Eng. Fract. Mech.* **2023**, *292*, 109649. [[CrossRef](#)]
54. Mohammadhosseini, H.; Yatim, J.M. Evaluation of the effective mechanical properties of concrete composites using industrial waste carpet fiber. *INAE Lett.* **2017**, *2*, 1–12. [[CrossRef](#)]
55. Jamshidi, M.; Karimi, M. Characterization of polymeric fibers as reinforcements of cement-based composites. *J. Appl. Polym. Sci.* **2010**, *115*, 2779–2785. [[CrossRef](#)]
56. Angelin, A.F.; Miranda, E.J.P.; Dos Santos, J.M.C.; Lintz, R.C.C.; Gachet-Barbosa, L.A. Rubberized mortar: The influence of aggregate granulometry in mechanical resistances and acoustic behavior. *Constr. Build. Mater.* **2019**, *200*, 248–254. [[CrossRef](#)]

57. Chen, L.J.; Zhang, X.X.; Liu, G.M. Analysis of dynamic mechanical properties of sprayed fiber-reinforced concrete based on the energy conversion principle. *Constr. Build. Mater.* **2020**, *254*, 119167. [[CrossRef](#)]
58. Du, B.; Ma, H.W.; Lin, L. Dynamic split tension and energy dissipation of fiber concrete under impact loading effect. In Proceedings of the International Conference on Electromechanical Control Technology and Transportation (ICECTT), Zhuhai, China, 31 October–1 November 2015; pp. 91–100.

**Disclaimer/Publisher’s Note:** The statements, opinions and data contained in all publications are solely those of the individual author(s) and contributor(s) and not of MDPI and/or the editor(s). MDPI and/or the editor(s) disclaim responsibility for any injury to people or property resulting from any ideas, methods, instructions or products referred to in the content.